Geophysical Journal International

*Geophys. J. Int.* (2024) **236,** 161–173 https://doi.org/10.1093/gji/ggad425
Advance Access publication 2023 October 30
GJI Seismology

# Assessing the effectiveness of the shear-tensile-compressive model in earthquake source inversions: synthetic experiments and field application

Yi Ren [1] Václav Vavryčuk [2,3] and Li Zhao [1]

[1] *School of Earth and Space Sciences, Peking University, Beijing* 100871*, China. E-mail: lizhaopku@pku.edu.cn*
[2] *Institute of Geophysics, The Czech Academy of Sciences, Boční II* 1401*,* 14100*, Praha* 4*, Czech Republic*
[3] *Institute of Geology, The Czech Academy of Sciences, Rozvojová* 269*,* 16500*, Praha* 6*, Czech Republic*

Accepted 2023 October 25. Received 2023 October 25; in original form 2023 May 4

## SUMMARY

As an alternative to the moment tensor (MT) model for earthquake sources, the shear-tensile-compressive (STC) model offers a kinematic description of the source mechanism and leads to a more robust inversion problem. However, the premise of the source inversion based on STC is to ensure the accuracy of parameter $\kappa$ defined as the ratio of the Lamé constants, $\kappa=\lambda/\mu$, in a fault zone. In this study, we carry out a series of synthetic experiments using *P*-wave amplitudes in source mechanism inversions based on both the STC and MT models, and consider the influence of noise, the uncertainties in source locations and in the velocity model. We show that the nonlinear STC inversion with an appropriate value of $\kappa$ leads to more accurate result compared to the linear MT inversion. We also propose a new joint-STC inversion method to jointly invert for parameter $\kappa$ and the remaining parameters of the STC model (magnitude and the strike, dip, rake and slope angles). The results indicate that our proposed method yields robust results for both the parameter $\kappa$ and focal mechanisms. We apply our joint-STC inversion method to field microearthquake data observed in the West Bohemia region to validate some of the conclusions drawn from the synthetic experiments.

**Key words:** Seismicity and tectonics; Earthquake source observations; Theoretical seismology.

## 1 INTRODUCTION

To gain information about seismic sources such as the orientations of activated fractures, modes of fracturing and the stress state in the focal zones, moment tensor (MT) is currently the most commonly adopted model (Dahlen & Tromp 1998; Aki & Richards 2002; Eyre & van der Baan 2017; Vavryčuk & Hrubcová 2017). Elements of the MT are linearly related to the observed seismic motions (e.g. Aki & Richards 2002). The MT model is often decomposed into double-couple (DC) and non-DC components (Knopoff & Randall 1970; Dahlen & Tromp 1998; Vavryčuk 2001, 2011; Tape & Tape 2013) in solving for the focal mechanism solutions (Jost & Herrmann 1989; Zhu & Ben-Zion 2013). The MT contains six independent parameters and it is not straightforward to interpret them in terms of the earthquake source processes (Jechumtálová *et al.* 2017). In addition, the inversion results are less reliable when the data are sparse or of low quality and are affected by uncertainties in earthquake locations and velocity models (Šílený *et al.* 1992; Šílený 2009; Stierle *et al.* 2014b; Ren *et al.* 2020).

The shear-tensile-compressive (STC) model, also referred to as the shear-tensile/implosion model (Pesicek *et al.* 2012) or general dislocation model (Li *et al.* 2021a) or other names (Vavryčuk 2001, 2011; Šílený & Horálek 2016), is an alternative model to describe earthquake sources. Besides the STC model, there are also other source models (e.g. Tape & Tape 2013). The STC model describes a shear slip which is accompanied by opening/closing along a fault plane. It was originally proposed by Kozák & Šílený (1985) with a focus on a tensile crack originating at the tip of a shear slip fault. It was also introduced by Dufumier and Rivera (1997) and later revisited by Vavryčuk (2001, 2011). The STC model is generally described by six parameters: two parameters (strike and dip angles) define the orientation of the fault plane, and two other parameters (rake and slope angles) define the slip direction. The fifth parameter is a product of the slip amplitude and the fault area or equivalently the event scalar moment. The sixth parameter involved in the STC model is $\kappa$, which is related to the properties of the medium. The strike, dip and rake angles define geometry of shear sources, whereas a non-zero slope angle (the angle between the slip vector and the fault plane) defines a non-shear source. The source is tensile (i.e. opening crack) for positive values of the slope, and compressive (i.e. closing crack) for negative values of the slope. The STC inversion has now been applied to obtain focal mechanisms

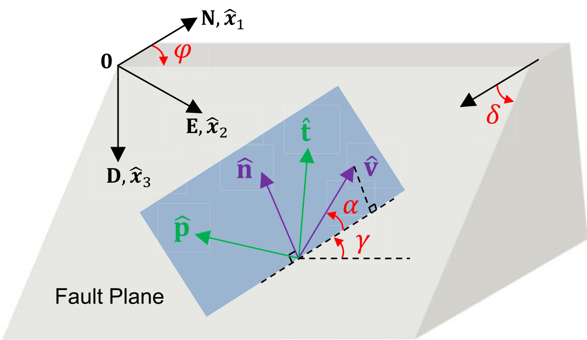


**Figure 1.** Geometry of the STC model is defined by four angles including strike $\varphi$, dip $\delta$, rake $\gamma$ and slope $\alpha$. Vector $\hat{\boldsymbol{n}}$ is the unit normal vector to the fault plane and vector $\hat{\boldsymbol{v}}$ is the unit slip vector. $\hat{\mathbf{p}}$ is the *P*-axis and $\hat{\mathbf{t}}$ is the *T*-axis. Note that the STC model reduces to a pure double couple when the slope angle $\alpha = 0°$.

and analyse the DC and non-DC components in volcanoes, microearthquake swarms, hydraulic fractures and laboratory rock experiments (Pesicek *et al.* 2012; Jechumtálová *et al.* 2014; Šílený *et al.* 2014; Šílený & Horálek 2016; Petružálek *et al.* 2018; Ren *et al.* 2021; Li *et al.* 2021a).

The parameter $\kappa$ can be defined in terms of the ratio between the Lamé parameters $\lambda$ and $\mu$, or between the *P*- and *S*-wave velocities $V_P$ and $V_S$, or the Poisson ratio $\nu$:

$$\kappa = \frac{\lambda}{\mu} = (V_P/V_S)^2 - 2 = \frac{2\nu}{1-2\nu}. \tag{1}$$

The lowest physically acceptable value for $\kappa$ is $-2/3$ (Vavryčuk 2001). If desired, the parameter $\kappa$ can be replaced by the Poisson ratio $\nu$. However, for the sake of consistency with previous studies on the STC model (e.g. Vavryčuk 2001, 2011), we stick with $\kappa$ in this study. Using seismic MTs and assuming the STC source model, Vavryčuk (2001) provided an independent estimation of $\kappa$ based on the evaluation of the ratio between the fractions (i.e. percentages) of the isotropic (ISO) and compensated linear vector dipole (CLVD) components $f^{\mathrm{ISO}}$ and $f^{\mathrm{CLVD}}$ (defined in Section 2.3):

$$\kappa = \frac{4}{3}\left(\frac{f^{\mathrm{ISO}}}{f^{\mathrm{CLVD}}} - \frac{1}{2}\right). \tag{2}$$

Since $\kappa$ in eq. (2) is calculated from parameters of faulting, it can be considered as a parameter describing the behaviour of the locally fractured medium near the fault (Vavryčuk 2001). However, the issue of whether $\kappa$ is a near-fault parameter or not is still under broad theoretical discussions (e.g. Vavryčuk 2011; Tape & Tape 2013). The differences between values of $\kappa$ determined from eqs (1) and (2) are caused by many factors, such as anomalous mechanical properties in the focal zone and errors in the source and velocity models. Vavryčuk (2011) later compared three methods for determining $\kappa$ based on the ISO and CLVD components obtained from MT inversions.

Stierle *et al.* (2014b) and Šílený *et al.* (2014) neglected the anomalous behaviour of $\kappa$ in the focal zone and conducted numerical experiments with STC inversions by setting the velocity ratio in eq. (1) with $V_P/V_S = \sqrt{3}$, which is the most commonly used value in crustal velocity models. The corresponding value for the $f^{\mathrm{ISO}}/f^{\mathrm{CLVD}}$ ratio is 1.25 according to eq. (2). However, when analysing source mechanisms of aftershocks (Stierle *et al.* 2014a), earthquake swarms (Vavryčuk *et al.* 2021), hydraulic fractures (Yu *et al.* 2018; Zhang *et al.* 2019) and laboratory rock failures (Davi *et al.* 2013; Stierle *et al.* 2016), it was found that the $f^{\mathrm{ISO}}/f^{\mathrm{CLVD}}$ values obtained by the MT inversions are systematically lower than 1.25. This makes $\kappa$ estimated from eq. (2) less than 1, and some of them even negative. Such low $\kappa$ values probably point to highly fractured rocks in the focal area (Vavryčuk *et al.* 2021).

This raises the following problems: how sensitive is the STC inversion to the value of $\kappa$? Is the STC inversion reasonably accurate even if a biased value of $\kappa$ is used? Do we need to apply a more sophisticated inversion when the parameters of the STC model are inverted jointly with parameter $\kappa$?

In order to resolve these problems, we carry out a series of synthetic experiments of the STC and MT inversions, in which the influence of noise on amplitudes and the uncertainties in source locations and in the velocity model are considered. The errors of source components and *P*/*T* axes are used to demonstrate the effectiveness of different inversion methods. The following issues are tested and discussed: (1) the effectiveness of the STC inversion is tested when an unreasonable $\kappa$ is used; (2) three different methods including a nonlinear joint-STC inversion approach proposed here are tested in solving for $\kappa$ and (3) the effectiveness of the MT and STC-joint inversions are compared and analysed. Finally, we use the microearthquake data recorded in the West Bohemia swarm area in the Czech Republic to verify some of the conclusions derived from the synthetic experiments. Our results shed a new light on the interpretation of earthquake source components and focal mechanisms.

## 2 METHODS

### 2.1 Linear MT inversion

The MT inversion is based on the linear relation between the seismic displacement amplitudes and the MTs of point sources:

$$\mathbf{u} = \mathbf{G}\mathbf{m}, \tag{3}$$

where $\mathbf{m}$ is the column vector composed of the six components of the MT:

$$\mathbf{m} = [m_{11}\ m_{22}\ m_{33}\ m_{12}\ m_{13}\ m_{23}]^T. \tag{4}$$

$\mathbf{u}$ is an *N*-component vector representing the *P*-wave first-motion amplitudes of vertical displacement records, with *N* the total number of amplitude measurements for a given event. $\mathbf{G}$ is the $N \times 6$ matrix containing the spatial gradient components of the Green's functions.

Adopting the least-squares method, the solution to the inverse problem in eq. (3) is

$$\mathbf{m} = (\mathbf{G}^T \cdot \mathbf{G})^{-1} \cdot \mathbf{G}^T \cdot \mathbf{u}. \tag{5}$$

### 2.2 STC inversion

As shown in Fig. 1, geometry of the STC model is described by four angles: strike $\varphi$, dip $\delta$, rake $\gamma$ and slope $\alpha$ (Vavryčuk 2001, 2011). The strike and dip angles define the orientation of the fault plane, whereas the rake and slope angles define the slip direction $\hat{\boldsymbol{v}}$. The slope angle $\alpha$ measures the deviation of the slip vector $\boldsymbol{v}$ from the fault plane, which is positive for a shear-tensile event and negative for a shear-compressive event. In the coordinate system $(\hat{\boldsymbol{x}}_1, \hat{\boldsymbol{x}}_2, \hat{\boldsymbol{x}}_3)$, with $\hat{\boldsymbol{x}}_1$, $\hat{\boldsymbol{x}}_2$ and $\hat{\boldsymbol{x}}_3$ defined as north, east and down, the normal vector $\hat{\boldsymbol{n}}$ and the slip direction $\hat{\boldsymbol{v}}$ are given by the angles $\varphi$, $\delta$, $\gamma$ and $\alpha$ as follows (Vavryčuk 2011):

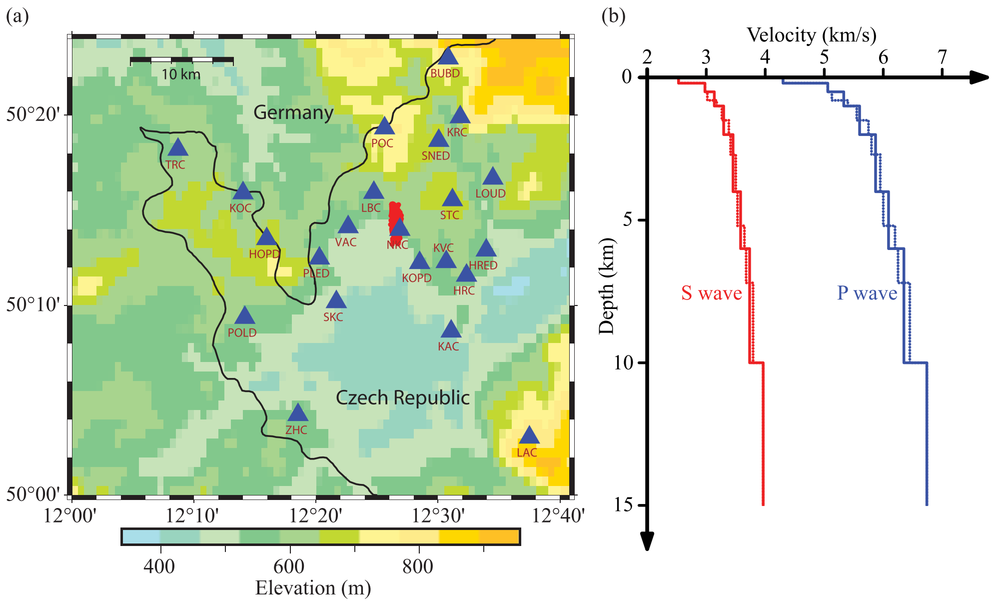


**Figure 2.** (a) Map of the West Bohemia region. The 4500 epicentres of the 2011 swarm including those of the 200 microearthquakes used in Section 4 are marked by red dots. The WEBNET stations are shown by blue triangles. The black line marks the border between Germany and the Czech Republic. (b) Velocity model for the West Bohemia region used in this study. The *P*- and *S*-wave velocities are shown by the blue and red solid lines, respectively. The blue and red dotted lines represent the *P*- and *S*-wave velocities, respectively, which are used in the inversion of Scenario II.

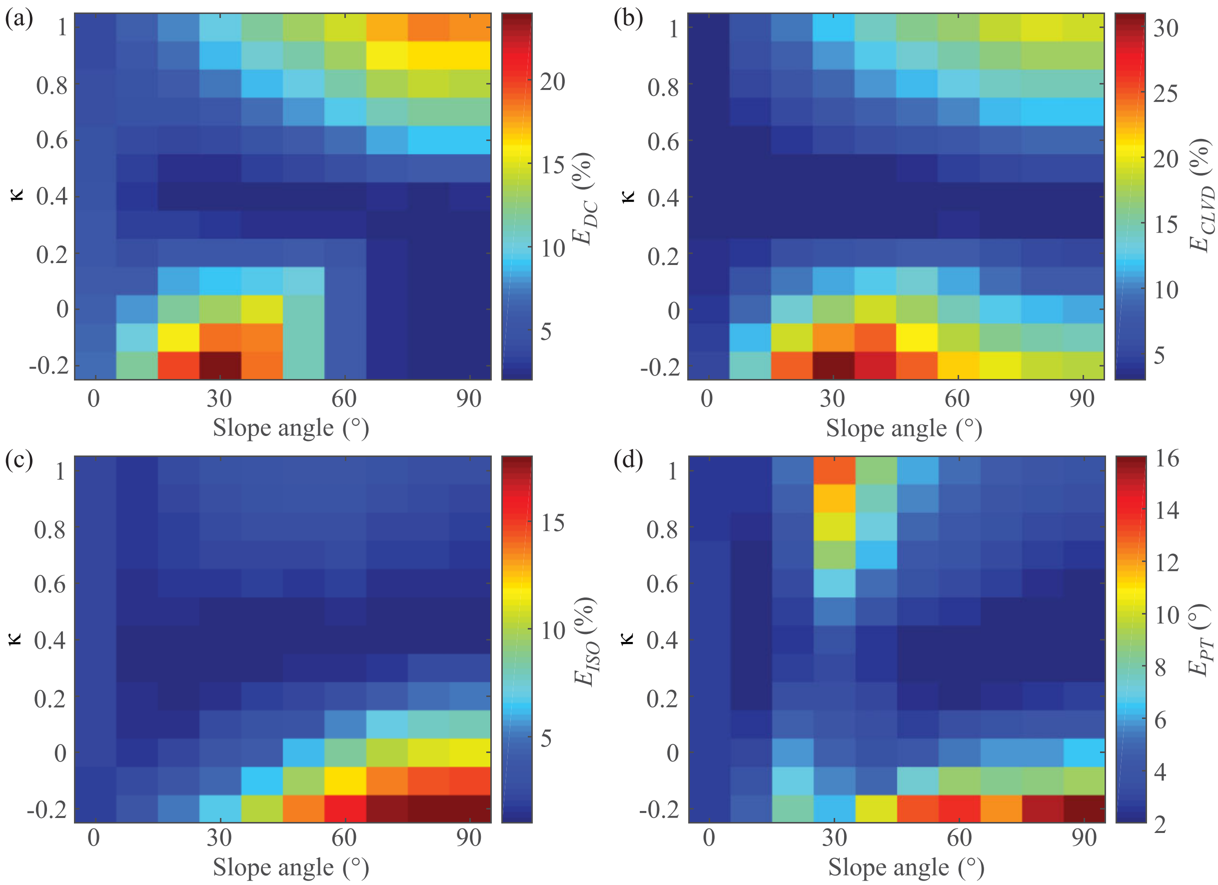


**Figure 3.** Variations of the errors with the slope angle and $\kappa$ values used in the STC inversions under Scenario I for the true value of $\kappa_0 = 0.4$. We use 200 synthetic microearthquakes in each inversion. Panels (a), (b), (c) and (d) are for $E_{\mathrm{DC}}$, $E_{\mathrm{CLVD}}$, $E_{\mathrm{ISO}}$ and $E_{PT}$, respectively. Note that the colour scales in (a)–(d) are different.

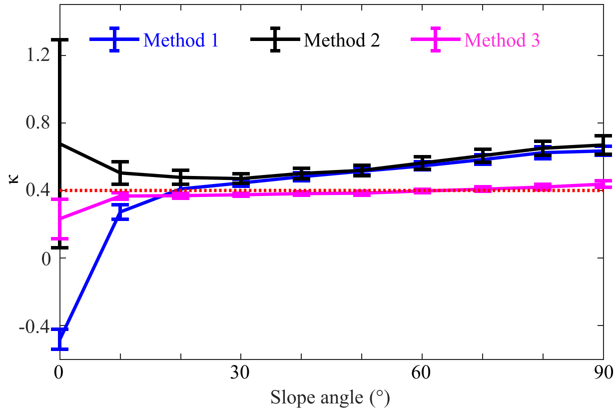


**Figure 4.** Variations of $\kappa$ obtained by using three different methods with the slope angle under Scenario I. Blue and black lines are for Methods 1 and 2, respectively. The magenta line is for Method 3 proposed in this study. Vertical bars show the corresponding standard deviations. The red dotted line shows the true value $\kappa_0 = 0.4$.

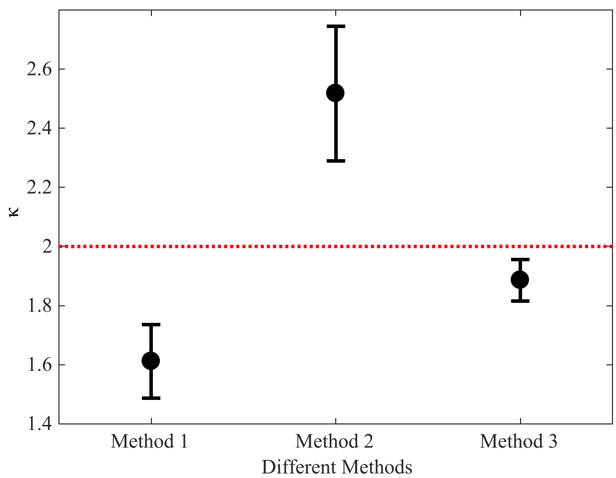


**Figure 5.** Comparison of the means and standard deviations for $\kappa$ obtained by different inversion methods for a relatively large true value $\kappa_0 = 2$ (dotted red line) under Scenario I. Each inversion involves 100 synthetic microearthquakes with randomly chosen slope angles in the range of 0°–30°.

$$\begin{aligned}\hat{n}_1 &= -\sin\delta\sin\varphi,\\ \hat{n}_2 &= \sin\delta\cos\varphi,\\ \hat{n}_3 &= -\cos\delta,\end{aligned}\tag{6}$$

$$\begin{aligned}\hat{v}_1 &= (\cos\gamma\cos\varphi + \cos\delta\sin\gamma\sin\varphi)\cos\alpha - \sin\delta\sin\varphi\sin\alpha,\\ \hat{v}_2 &= (\cos\gamma\sin\varphi - \cos\delta\sin\gamma\cos\varphi)\cos\alpha + \sin\delta\cos\varphi\sin\alpha,\\ \hat{v}_3 &= -\sin\gamma\sin\delta\cos\alpha - \cos\delta\sin\alpha.\end{aligned}\tag{7}$$

The MT for a point source in an ISO medium is expressed as (Vavryčuk 2011):

$$\begin{aligned}m_{ij} &= uS\left[\lambda\hat{n}_k\hat{v}_k\delta_{ij} + \mu\left(\hat{n}_i\hat{v}_j + \hat{n}_j\hat{v}_i\right)\right]\\ &= \mu uS\left(\kappa\sin\alpha\delta_{ij} + \hat{n}_i\hat{v}_j + \hat{n}_j\hat{v}_i\right),\end{aligned}\tag{8}$$

where $u$ is the length of the slip vector, $S$ is the fault area, and we have used the relation $\hat{n}_k\hat{v}_k = \sin\alpha$, and $\delta_{ij}$ is the Kronecker delta.

Inserting eqs (6) and (7) into eq. (8), we obtain the six components of the MT, with the three diagonal elements related to the parameter $\kappa$:

$$m_{11} = \mu uS\left[\left(\kappa + 2\sin^2\delta\sin^2\varphi\right)\sin\alpha - \left(\sin\delta\cos\gamma\sin 2\varphi + \sin 2\delta\sin\gamma\sin^2\varphi\right)\cos\alpha\right],\tag{9}$$

$$m_{22} = \mu uS\left[\left(\kappa + 2\sin^2\delta\cos^2\varphi\right)\sin\alpha + \left(\sin\delta\cos\gamma\sin 2\varphi - \sin 2\delta\sin\gamma\cos^2\varphi\right)\cos\alpha\right],\tag{10}$$

$$m_{33} = u\mu S\left[\left(\kappa + 2\cos^2\delta\right)\sin\alpha + \sin 2\delta\sin\gamma\cos\alpha\right],\tag{11}$$

$$\begin{aligned}m_{12} = \mu uS\big[&-2\sin^2\delta\sin 2\varphi\sin\alpha\\ &+ (\sin\delta\cos\gamma\cos 2\varphi + 0.5\sin 2\delta\sin\gamma\sin 2\varphi)\cos\alpha\big],\end{aligned}\tag{12}$$

$$m_{13} = \mu uS\left[\sin 2\delta\sin\varphi\sin\alpha - (\cos\delta\cos\gamma\cos\varphi + \cos 2\delta\sin\gamma\sin\varphi)\cos\alpha\right],\tag{13}$$

$$m_{23} = \mu uS\left[-\sin 2\delta\cos\varphi\sin\alpha - (\cos\delta\cos\gamma\sin\varphi - \cos 2\delta\sin\gamma\cos\varphi)\cos\alpha\right].\tag{14}$$

The vectors $\hat{\boldsymbol{n}}$ and $\hat{\boldsymbol{v}}$ can be expressed as (Vavryčuk 2011):

$$\hat{\boldsymbol{n}} = \sqrt{\frac{M_1 - M_2}{M_1 - M_3}}\hat{\mathbf{e}}_1 + \sqrt{\frac{M_3 - M_2}{M_3 - M_1}}\hat{\mathbf{e}}_3,\tag{15}$$

$$\hat{\boldsymbol{v}} = \sqrt{\frac{M_1 - M_2}{M_1 - M_3}}\hat{\mathbf{e}}_1 - \sqrt{\frac{M_3 - M_2}{M_3 - M_1}}\hat{\mathbf{e}}_3,\tag{16}$$

where $M_1 \geq M_2 \geq M_3$ are the eigenvalues of the MT, and $\hat{\mathbf{e}}_1$, $\hat{\mathbf{e}}_2$ and $\hat{\mathbf{e}}_3$ are the corresponding normalized eigenvectors, which also define the *T*-, *B*- and *P*-axes, respectively. Physically, the *P*- and *T*-axes specify directions of the maximum compressional and tensional axes at the source, respectively, which are often used to characterize the orientation of a DC source mechanism.

The STC inversion is a nonlinear problem and can be solved by a number of well-established optimization methods in which the misfit between the model-predicted and observed amplitudes is minimized. The predicted amplitudes can be calculated by the Green's functions (e.g. Aki & Richards 2002) and the MTs of source models. Both the model-predicted and observed amplitudes in the STC inversions are normalized, which means that the product $uS$ related to the scalar moment of the event is not inverted for in the nonlinear inversion process. Combining eqs (9)–(14), and eqs (3) and (4) can relate the amplitude $\mathbf{u}$ with the source parameters (four angles and $\kappa$) to be inverted. Here, we adopt the interior-point algorithm, which uses the conjugate gradient method to iteratively find the minimum within prescribed limits (Byrd *et al.* 2000). A grid search is an alternative but is also unnecessarily time consuming. The interior-point algorithm is more efficient and yields reliable results. In this study, the parameter limits are set as follows: $0 \leq \varphi \leq 360°$, $0 \leq \delta \leq 90°$, $-180° \leq \gamma \leq 180°$ and $-90° \leq \alpha \leq 90°$. In Section 3.2, we test the impact of biased values of $\kappa$ on the inversion results by assuming a variety of fixed values of $\kappa$; and in Section 3.3, we explore how to obtain robust estimation for the value of $\kappa$.

## 2.3 Decomposition of moment tensor

Following Vavryčuk (2001, 2011), the MT is usually decomposed into the ISO, DC and CLVD components as follows:

$$\mathbf{m} = \mathbf{m}^{\mathrm{I}} + \mathbf{m}^{\mathrm{D}} = \mathbf{m}^{\mathrm{I}} + \mathbf{m}^{\mathrm{DC}} + \mathbf{m}^{\mathrm{CLVD}},\tag{17}$$

$$\mathbf{m}^{\mathrm{I}} = \frac{1}{3}\mathrm{tr}(\mathbf{m})\begin{bmatrix}1 & 0 & 0\\ 0 & 1 & 0\\ 0 & 0 & 1\end{bmatrix},\tag{18}$$

$$\mathbf{m}^{\mathrm{DC}} = (1 - 2|\varepsilon|)\,M_{|\max|}\begin{bmatrix}-1 & 0 & 0\\ 0 & 0 & 0\\ 0 & 0 & 1\end{bmatrix},\tag{19}$$

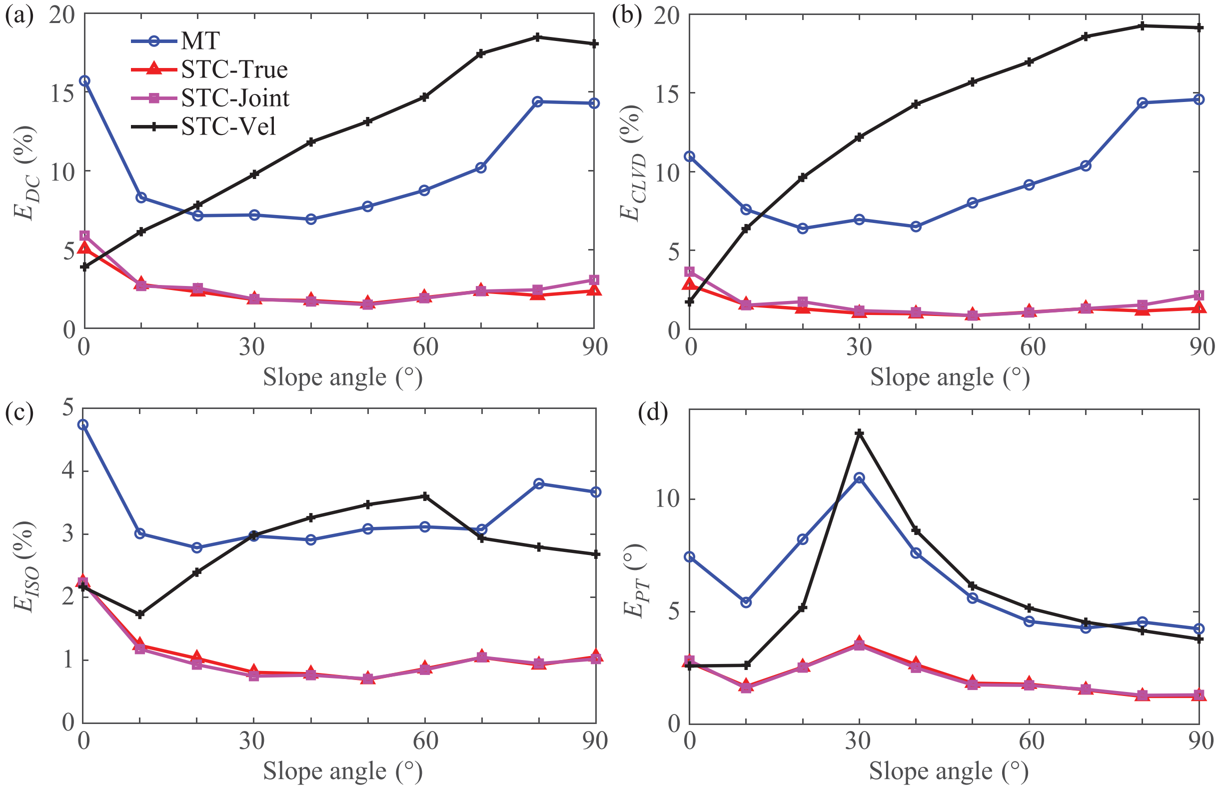


**Figure 6.** Variations of (a) $E_{\mathrm{DC}}$, (b) $E_{\mathrm{CLVD}}$, (c) $E_{ISO}$ and (d) $E_{PT}$ with the slope angle under Scenario I. Blue lines show the results for the MT inversion. Red, magenta and black lines show results for inversion strategies of STC-True, STC-Joint and STC-Vel, respectively. 200 synthetic microearthquakes are used. Note that the vertical scales in (a)–(d) are different.

$$\mathbf{m}^{\mathrm{CLVD}} = |\varepsilon|\, M_{|\max|} \begin{bmatrix} -1 & 0 & 0 \\ 0 & -1 & 0 \\ 0 & 0 & 2 \end{bmatrix}, \tag{20}$$

$$\varepsilon = -\frac{M_{|\min|}}{\left|M_{|\max|}\right|}, \tag{21}$$

where $\mathbf{m}^{\mathrm{I}}$ and $\mathbf{m}^{\mathrm{D}}$ represent the ISO and deviatoric parts of the MT, respectively. The symbol $\mathrm{tr}(\cdot)$ stands for the trace of a matrix. $\mathbf{m}^{\mathrm{DC}}$ and $\mathbf{m}^{\mathrm{CLVD}}$ are the DC and CLVD components of the deviatoric part. $M_{|\max|}$ and $M_{|\min|}$ are the eigenvalues of the deviatoric part $\mathbf{m}^{\mathrm{D}}$ with the biggest and smallest absolute values, respectively. The fractions of the ISO, DC and CLVD components in an MT can be evaluated as follows:

$$f^{\mathrm{ISO}} = \frac{1}{3}\frac{\mathrm{tr}(\mathbf{m})}{\left|M_{|\max|}\right|}, \tag{22}$$

$$f^{\mathrm{CLVD}} = 2\varepsilon\left(1 - \left|f^{\mathrm{ISO}}\right|\right), \tag{23}$$

$$f^{\mathrm{DC}} = 1 - \left|f^{\mathrm{ISO}}\right| - \left|f^{\mathrm{CLVD}}\right|. \tag{24}$$

For a purely shear event, the fraction (percentage) of the DC component is 100 per cent, whereas it is zero for a purely tensile event. It should be noted that the above MT decomposition is not the only decomposition used in the literature. For a review, see Vavryčuk (2015a).

### 2.4 Estimation of $\kappa$

Vavryčuk (2011) described different methods to solve for $\kappa$ in a source region based on the MT solutions of local events. Here, we consider two methods:

Method 1. We first solve a linear inverse problem for the MT of each event. Then a linear regression (Weisberg 2013) between the ISO and CLVD fractions is conducted collectively from all events with the constrain that the regression line runs through the origin ($f^{\mathrm{ISO}} = f^{\mathrm{CLVD}} = 0$). Then, $\kappa$ is calculated from the ratio $f^{\mathrm{ISO}}/f^{\mathrm{CLVD}}$ by eq. (2).

Method 2. Again, first we solve a linear inverse problem for the MT of each event. Then, we minimize the misfit function (for details, see Vavryčuk 2011):

$$\sum_{i=1}^{L}\left|\frac{M_2 - c\cdot\mathrm{tr}(\mathbf{m})}{M_1 - M_3}\right|_i = \min, \tag{25}$$

where

$$c = \frac{\kappa}{3\kappa + 2}. \tag{26}$$

As in Method 1, the minimization is performed involving all events.

Method 3. Here, we propose a third method, which is a joint inversion for $\kappa$ and for parameters defining the STC model. In other words, we now consider the STC model as a six-parameter model (angles $\varphi$, $\delta$, $\gamma$ and $\alpha$, parameter $\kappa$ and the product $uS$). Again, the inversion involves all events and the joint nonlinear L1-norm minimization of the objective function is defined as:

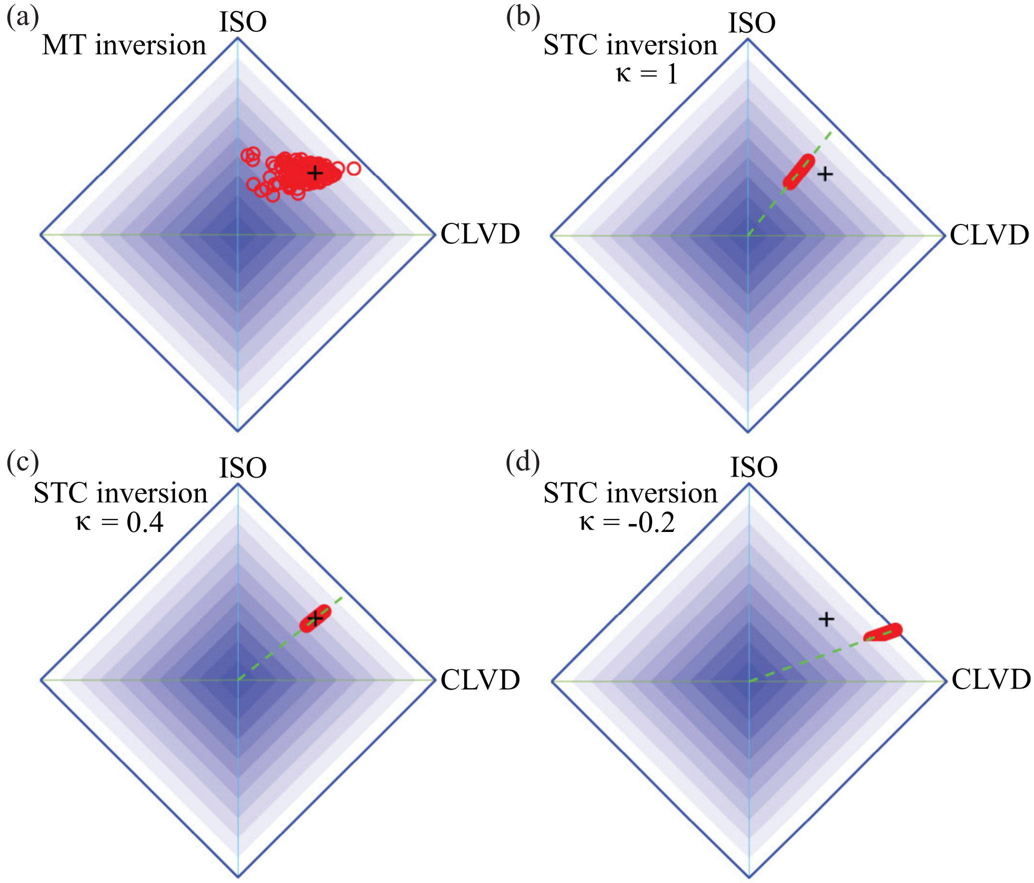


**Figure 7.** The CLVD–ISO diamond plots for synthetic experiment results (red circles) obtained from four different inversion strategies for a slope angle of 30° under Scenario I. (a) MT inversion; (b) STC inversion using $\kappa = 1$; (c) STC inversion using $\kappa = 0.4$, which is the true value of $\kappa$ and (d) STC inversion using $\kappa = -0.2$. The black plus sign in each plot represents the true position of the assumed source. In (b)–(d), the green dotted lines represent all the possibilities for the distribution of the events in the diamond plot when $\kappa$ is fixed and the slope angle is greater than or equal to 0°. 200 synthetic microearthquakes are used for each inversion strategy. Note that the results can also be displayed by other graphical representations of the source components such as the lune plot (e.g. Chapman & Leaney 2012; Tape & Tape 2012a,b).

$$\varepsilon_i^{\kappa} = \frac{1}{N_i}\sum_{j=1}^{N_i}\left|u_{ij}^{\mathrm{the}}\left(\varphi_i, \delta_i, \gamma_i, \alpha_i, \kappa\right) - u_{ij}^{\mathrm{obs}}\right|, \tag{27}$$

$$\frac{1}{L}\sum_{i=1}^{L}\varepsilon_i^{\kappa} = \min, \tag{28}$$

where $N_i$ is the number of amplitude measurements for the $i$th event, $L$ is the number of local events, $\varepsilon_i^{\kappa}$ is the residual of the STC inversion for the $i$th event and $u_{ij}^{\mathrm{the}}(\varphi_i, \delta_i, \gamma_i, \alpha_i, \kappa)$ and $u_{ij}^{\mathrm{obs}}$ are the $j$th theoretical and observed amplitudes for the $i$th event, respectively. The basic advantage of Method 3 is that it uses jointly all the events and amplitudes involved. It does not need an intermediate stage of solving for the MTs. The method directly employs the observed amplitudes to solve for $\kappa$, thus reducing the errors caused by the conversions of intermediate parameters and resulting in a more accurate $\kappa$. Besides, the joint inversion can better reflect a complex relation between $\kappa$ and the focal mechanisms of all events.

In the implementation of Method 3, the value of $\kappa$ is first assumed to be known and the same for all events in the inversion. For example, we can take the value of $\kappa$ between $-0.6$ and 1 with an interval of 0.01, resulting in a total of 161 $\kappa$ samples. Secondly, for each sample of $\kappa$, we invert for the focal mechanism of the $i$th event and calculate the residual $\varepsilon_i$ based on eq. (27). Then, the average residual for all events can be calculated from the left-hand side of eq. (28). Thirdly, the value of $\kappa$ corresponding to the minimum average residual for all events in the 161 samples is the optimal value (detailed later in Fig. S2 Supporting Information), and the corresponding focal mechanism is also optimal. The interior-point algorithm is used for minimizing the objective function in eqs (27) and (28), and the ranges for the parameters (strike/dip/rake/slope) are the same as those in Section 2.2.

## 3 SYNTHETIC EXPERIMENTS

### 3.1 Setup of synthetic experiments

To ensure the applicability of our proposed method, we first conduct inversion experiments using synthetic data generated in a realistic source-station configuration. Therefore, we use the station distribution and the $V_P$ and $V_S$ models in the West Bohemia region (Fig. 2) where earthquake swarms occur frequently and the local West Bohemia Network (WEBNET) has been deployed for the purpose of monitoring the local seismic activity (Růžek & Horálek 2013; Bachura & Fischer 2016; Valentová *et al.* 2017; Vavryčuk *et al.* 2021). We use a layered ISO model, because seismic anisotropy is weak in the area (Růžek *et al.* 2003) and numerical tests indicate

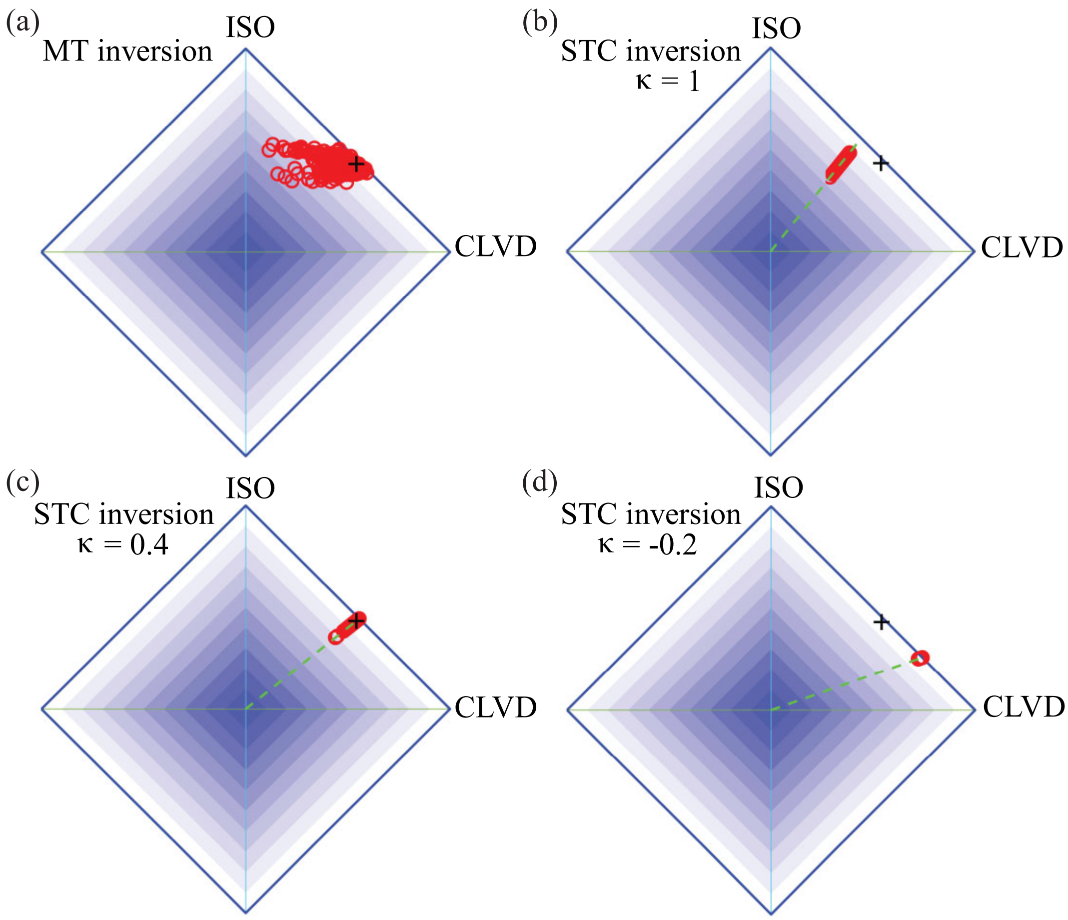


**Figure 8.** Same as Fig. 7, but for a slope angle of 70°.

that errors produced by its neglect should be insignificant (Šílený & Vavryčuk 2002). The network covers the earthquake swarm area with no significant azimuthal gaps. The velocity ratio in the ISO crustal model (used for calculating Green's functions) is assumed to be $V_P/V_S = \sqrt{3}$ with a parameter $\kappa$ of 1. When using the STC model, we should consider a specific value of $\kappa$ different from 1 in the fault zone.

For the synthetic experiments, the events are randomly distributed in a 2 km × 2 km × 2 km volume, with its centre at 12.44° E longitude, 50.24° N latitude and 9 km depth. The Green's functions are calculated for the 1-D layered model using the ray method (Červený 2001). The synthetic amplitudes are obtained from the Green's functions and MTs according to eq. (3). In each experiment, we invert for 200 (Sections 3.2 and 3.4) or 100 (Section 3.3) synthetic microearthquakes of similar focal mechanisms with strike, dip and rake angles randomly generated and uniformly distributed in the intervals of 160° ± 10°, 80° ± 5° and − 30° ± 10°, respectively. These focal mechanisms are similar to one of the typical focal mechanisms in the West Bohemia area (Vavryčuk *et al.* 2021, 2022) being well oriented with respect to the regional stress field. The slope angle is fixed in each inversion experiment, and we test the slope angles from 0° (pure shear) to 90° (pure tensile) at an interval of 10°, resulting in a total of 10 experiments. The parameter $\kappa$ is set to a fixed (true) value $\kappa_0$ =0.4 for all synthetic microearthquakes, which is also used in computing (a) the MTs based on eqs (8)–(11). The moment magnitude ($M_{\mathrm{w}}$) of each synthetic event is 1.

In the synthetic tests, we introduce two scenarios that simulate the loss of data quality and/or quantity as well as biases in the inversions. In Scenario I (Sections 3.2–3.4), the amplitudes are contaminated by Gaussian noise, with the noise level depending on the length of ray path from source to station (Stierle *et al.* 2014b). In Scenario II (Section 3.4), in addition to the noise contamination in Scenario I, the events are mislocated systematically by 500 m vertically and 300 m horizontally (in random azimuths) from the true positions (Šílený 2009); the *P*- and *S*-wave velocities are perturbed as shown by the dotted lines in Fig. 2(b); meanwhile, amplitudes are not used at eight randomly selected stations for each event. The second scenario represents a typical situation of microearthquake data, in which seismic noise, location and velocity errors and data loss coexist.

We quantify the inversion error by two types of measures. One is the averaged absolute values of the differences in the percentages of the DC, CLVD and ISO components, denoted by $E_{\mathrm{DC}}$, $E_{\mathrm{CLVD}}$ and $E_{\mathrm{ISO}}$, respectively, between the true percentages of the DC ($f_i^{\mathrm{DC}}$), CLVD ($f_i^{\mathrm{CLVD}}$) and ISO ($f_i^{\mathrm{ISO}}$) components and the corresponding inverted percentages $\tilde{f}_i^{\mathrm{DC}}$, $\tilde{f}_i^{\mathrm{CLVD}}$ and $\tilde{f}_i^{\mathrm{ISO}}$ (Stierle *et al.* 2014b; Ren

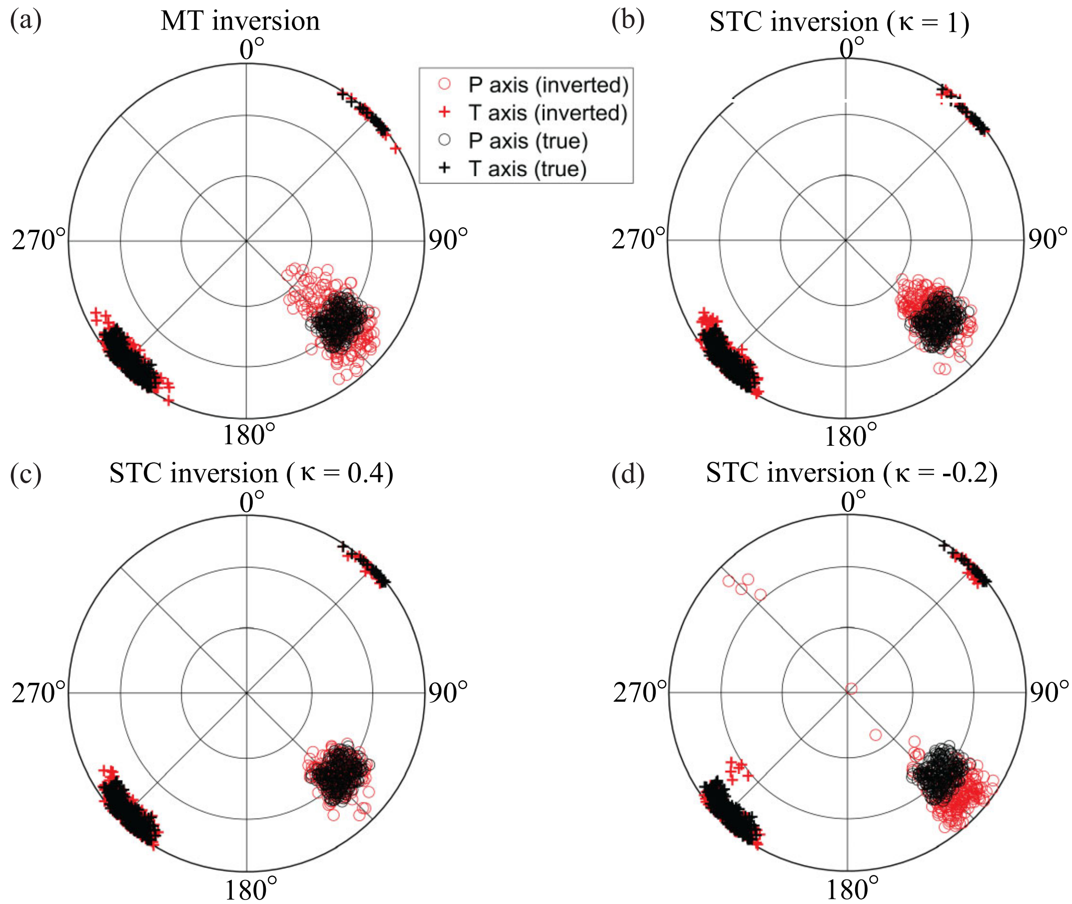


**Figure 9.** Plots of *P*- and *T*-axes for the results from four different inversion strategies for a slope angle of 30° under Scenario I. (a) MT inversion; (b) STC inversion using $\kappa = 1$; (c) STC inversion using $\kappa = 0.4$, which is the true value of $\kappa$ and (d) STC inversion using $\kappa = -0.2$. In each subplot, the black plus signs and circles in each plot represent the true positions of the *T*- and *P*-axes, respectively; whereas the red plus signs and circles represent the positions of the *T*- and *P*-axes, respectively, from the inversions.

*et al.* 2020):

$$E_{\mathrm{DC}} = \frac{1}{L}\sum_{i=1}^{L}\left|f_i^{\mathrm{DC}} - \tilde{f}_i^{\mathrm{DC}}\right|,$$

$$E_{\mathrm{CLVD}} = \frac{1}{L}\sum_{i=1}^{L}\left|f_i^{\mathrm{CLVD}} - \tilde{f}_i^{\mathrm{CLVD}}\right|,$$

$$E_{\mathrm{ISO}} = \frac{1}{L}\sum_{i=1}^{L}\left|f_i^{\mathrm{ISO}} - \tilde{f}_i^{\mathrm{ISO}}\right|. \tag{29}$$

The second type of measure for inversion error is the average deviation angle $E_{PT}$ between the true and inverted *P*- and *T*-axes (Vavryčuk *et al.* 2017) defined as:

$$E_{PT} = \frac{1}{L}\sum_{i=1}^{L}\frac{1}{2}\left[\cos^{-1}\left(\hat{\mathbf{p}}_i \cdot \widehat{\tilde{\mathbf{p}}}_i\right) + \cos^{-1}\left(\hat{\mathbf{t}}_i \cdot \widehat{\tilde{\mathbf{t}}}_i\right)\right], \tag{30}$$

where $\hat{\mathbf{p}}_i$ and $\hat{\mathbf{t}}_i$ are the unit vectors for the true *P*- and *T*-axes, respectively, of the *i*th event; $\widehat{\tilde{\mathbf{p}}}_i$ and $\widehat{\tilde{\mathbf{t}}}_i$ are the corresponding inversion results. The rotation angle can also be estimated by the Kagan (1991) angle, which quantifies the minimum rotation angle between two sets of coordinate systems. However, in the analysis of a large number of microearthquakes, eq. (30) is straightforward and intuitively defines the errors in focal mechanisms and biases of the *P*- and *T*-axes, which are beneficial for analysing the disturbance of the stress field.

The four quantities defined in eqs (29) and (30) provide a comprehensive measure of the biases in the DC and non-DC characteristics of the inversion results.

## 3.2 The effect of $\kappa$ on STC inversion

We first test the effect of an inappropriate value of $\kappa$ on the STC inversion under Scenario I. As stated before, we conduct 10 inversion experiments with 10 different slope angles, with each experiment involving 200 synthetic microearthquakes having the same slope angle. Different values of $\kappa$ ranging from $-0.2$ to 1 with an interval of 0.1 are tested in the STC inversion in each experiment with a true value of $\kappa_0 = 0.4$. Fig. 3 shows the variations of the four types of inversion errors defined in eqs (29) and (30) with the slope angle $\alpha$ for different $\kappa$ values used in the STC inversions. It shows that using an inappropriate $\kappa$ value affects the STC inversion significantly. The results of the cases where the slope angles are negative are shown in the Fig. S1 in the Supporting Information, and most of the results are similar to those in Fig. 3.

Fig. 3 shows that when the value of $\kappa$ is between 0.3 and 0.5 (i.e. close to the true value of 0.4), most of the error measures are small for all slope angles. The differences are less than 5 per cent

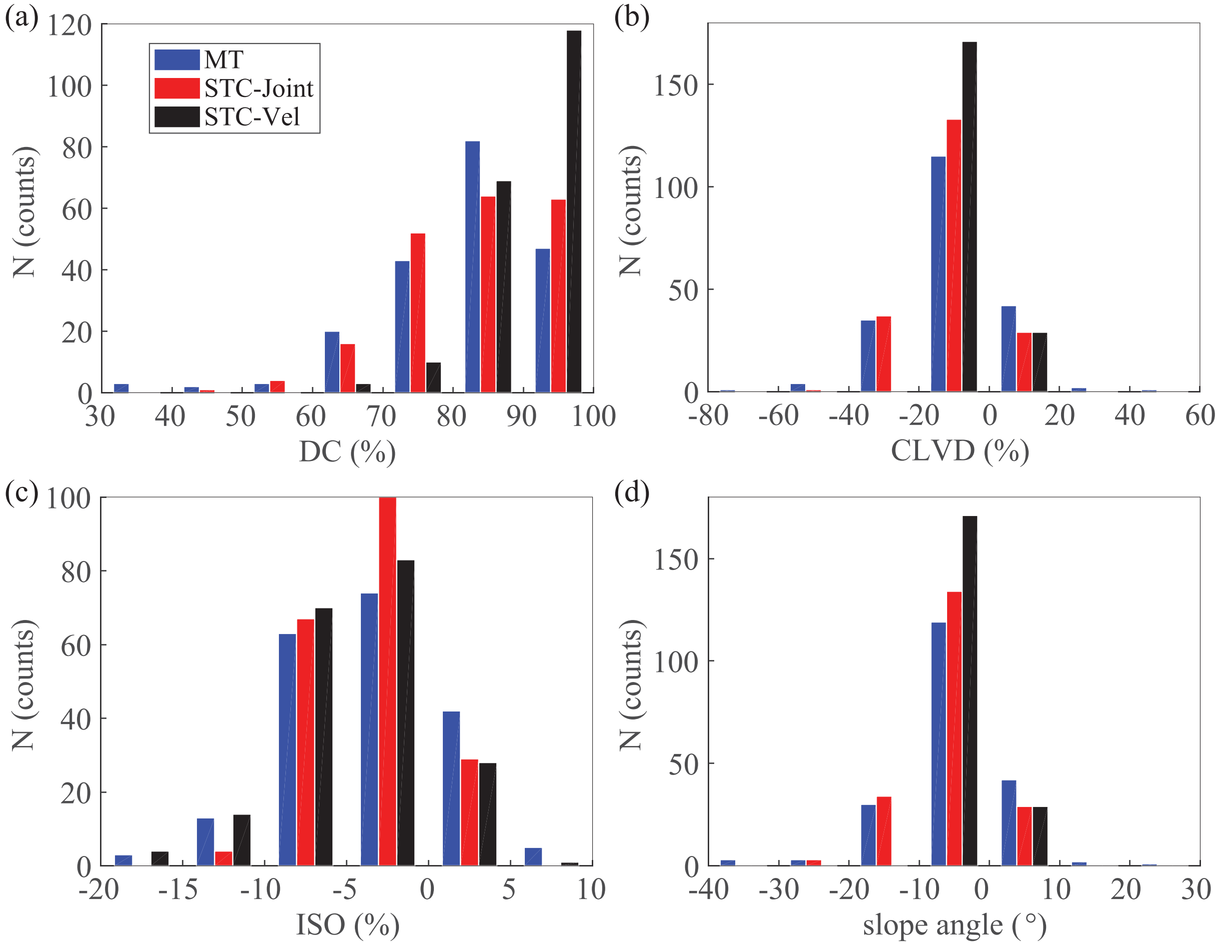


**Figure 10.** Statistics of the (a) DC, (b) CLVD, (c) ISO components and (d) the slope angles of the selected 200 microearthquakes in the West Bohemia region obtained from three different inversion strategies. Blue: MT inversion; red: STC-Joint inversion and black: STC-Vel inversion.

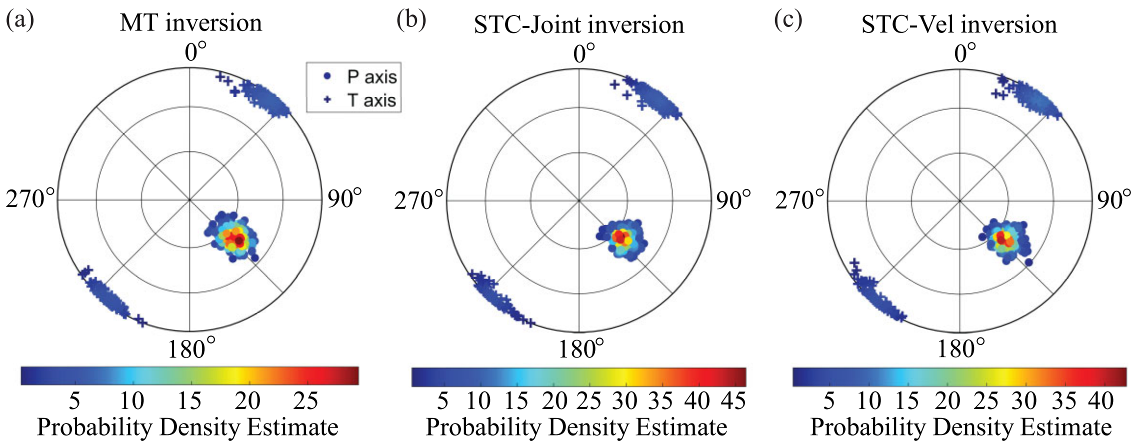


**Figure 11.** Distributions and probability density estimations of the *P*- and *T*-axes corresponding to three different inversion strategies: (a) MT inversion; (b) STC-Joint inversion and (c) STC-Vel inversion. The events are the same as those in Fig. 10. Plus signs are for the *T*-axis and dots are for the *P*-axis. Lower hemisphere equal-area projection is used. Probability density estimation increases from blue to red. Note that the colour scales in (a)–(c) are different.

between the true and inverted DC, CLVD and ISO components and less than 5° between the true and inverted *P*- and *T*-axes. When $\kappa$ is large, $E_{\rm DC}$ and $E_{\rm CLVD}$ increase with the slope angle, and both have maximum values of about 18 per cent near $\kappa = 1$. In the meantime, $E_{\rm ISO}$ remains at a low level, while $E_{PT}$ reaches a maximum of about 12° when the slope angle is near 30°. An important observation in Fig. 3 is that when the slope angle is close to 0° (i.e. for purely shear events), all differences are small no matter what $\kappa$ is.

On the other hand, when $\kappa$ is small, the situation is quite different. $E_{\rm DC}$ and $E_{\rm CLVD}$ increase initially with the slope angle, reaching values of about 24 per cent and 30 per cent, respectively, at the slope of 30°, and then decrease. $E_{\rm ISO}$ and $E_{PT}$ monotonically increase with the slope angle. This suggests that how to obtain accurate $\kappa$ is the key point for subsequent solution of DC/CLVD/ISO components and *P*- and *T*-axes distribution.

### 3.3 Accuracy of different methods in solving for $\kappa$

Here, we solve for the value of $\kappa$ using all three methods described in Section 2.4 and compare the results. As described before, we conduct 10 experiments with 10 slope angles under Scenario I, with each experiment involving 100 synthetic microearthquakes. Considering the randomness of noise, each experiment is repeated 50 times to obtain the means and standard deviations. Fig. 4 shows the variations of the means and standard deviations of the three methods in solving for $\kappa$ with the slope angle. The true value is still $\kappa_0 = 0.4$, shown by the red dotted line in Fig. 4. Obviously, Method 3 (proposed in this study) yields $\kappa$ that is closest to the true value for all slope angles. Except for the case where slope angle is equal to 0°, the errors of $\kappa$ obtained using Method 3 are all within 10 per cent of the true value of $\kappa$. As the slope angle increases, the values of $\kappa$ obtained by Methods 1 and 2 also increase. For events with large slope angles, for example, 80°, the values of $\kappa$ estimated by Methods 1 and 2 are about 0.2 above the true value. Even for this modest error in $\kappa$, the biases in the DC and CLVD components become quite large (Figs 3a and b). For purely shear events ($\alpha = 0°$), the result of Method 3 also has a relatively large standard deviation. Fig. S2 (Supporting Information) shows details of obtaining $\kappa$ by using Method 3.

Vavryčuk (2011) conducted a numerical test about the effect of the $V_P/V_S$ ratio in the fault vicinity on the CLVD and ISO components of earthquakes. His results showed that when the true $V_P/V_S$ ratio is small (e.g. ~1.4), the estimation errors by Methods 1 and 2 are very small. However, when the true velocity ratio is large (e.g. 2.0), the estimation errors by the two methods are also quite large. Here, we demonstrate the same behaviour when considering $\kappa$ instead of $V_P/V_S$, as shown by the experiment in Fig. 5. This experiment evaluates the performance of the three methods in solving for a large value of $\kappa$ or $V_P/V_S$ ratio. In this experiment, we use 100 synthetic microearthquakes under Scenario I and repeat 50 times to obtain the means and standard deviations. The true value of $\kappa$ is set to 2, corresponding to $V_P/V_S = 2$. Instead of using fixed slope angles, the angles are randomly selected in the range of 0°–30°. The results show that the value of $\kappa$ obtained by our proposed Method 3 is still closest to the true value.

### 3.4 Comparison of MT and STC inversions

The synthetic experiments described in the previous sections demonstrate that an appropriate value of $\kappa$ ensures the accuracy of the STC inversion. In the experiments in this section, we compare the accuracy of the STC inversion with the results from the linear MT inversion. As stated before, we conduct 10 experiments for 10 different slope angles, with each experiment involving 200 synthetic microearthquakes. Both Scenarios I and II are considered in each experiment.

The MT inversion method adopted here uses the least-squares algorithm defined in eq. (5). For STC inversions, three different strategies are adopted: (1) STC-True, in which the true value of 0.4 for $\kappa$ is used; (2) STC-Joint, in which $\kappa$ is determined by our Method 3 and (3) STC-Vel, in which the standard velocity ratio of $V_P/V_S = \sqrt{3}$ is used to define $\kappa$.

The results are shown in Fig. 6 for Scenario I and in Fig. S3 (Supporting Information) for Scenario II. The results are similar for both scenarios. The four different biases by STC-True and STC-Joint have similar variations with the varying slope angle, and both are significantly lower than those by the MT inversion. In the results of the STC-Joint inversion, errors $E_{DC}$, $E_{CLVD}$ and $E_{ISO}$ are largest when the slope angle is close to 0°. However, the maximum $E_{PT}$ occurs when the slope angle is 30°. In almost all cases, the STC-Joint inversion yields the most accurate inversion results.

The results of the STC-Vel are quite complicated. It yields the smallest $E_{DC}$ and $E_{CLVD}$ among the four inversion strategies for pure shear events, and its $E_{ISO}$ and $E_{PT}$ are similar to those of the STC-True and STC-Joint inversions. However, for slope angles of a few degrees and larger, the errors of the STC-Vel inversion increase drastically, especially as measured by $E_{DC}$ and $E_{CLVD}$, being comparable to those of the MT inversions, and $E_{ISO}$ and $E_{PT}$ are also higher than those of the STC-Joint for shear-tensile or pure tensile events.

### 3.5 Further discussion on the synthetic experiment results using an incorrect $\kappa$

Let us further examine the inversion errors shown in Fig. 3. In Fig. 7, we plot the Hudson-type CLVD–ISO diamond diagram (Vavryčuk 2015a,b) for a slope angle of 30°. In this case, $f^{DC} = 29.4$ per cent, $f^{CLVD} = 39.2$ per cent and $f^{ISO} = 31.4$ per cent. The CLVD and ISO components are shown clearly in the CLVD–ISO coordinate system. The centre of the diamond represents a purely DC event, and the blue colour is used as a visual aid. The darker the colour, the larger the DC component. The DC components obtained by the STC inversion with a fixed value of $\kappa = 1$ are generally larger than the true values, whereas the situation is completely opposite when $\kappa = -0.2$. If the value of $\kappa$ is more accurate (i.e. near the true $\kappa_0 = 0.4$), the DC components obtained by the STC inversion are concentrated around the true value. Fig. 8 shows the diamond plots for the slope angle of 70°.

For shear-tensile events, it is straightforward that the larger the slope angle, the smaller the DC component. As indicated by eqs (9)–(11), if the value of $\kappa$ is limited to 1 in the STC inversion, which is larger than the true value, the slope angle $\alpha$ has a tendency to be underestimated in the inversion process. This is a compensation for an unreasonably large $\kappa$, as shown in Figs 7(b) and 8(b). Hence, the slope angle obtained by the STC inversion using $\kappa = 1$ is generally lower than the true slope angle, which results in an excessively large DC component. This is acceptable in solving for events with large DC components, especially for purely shear events with nearly 100 per cent DC component. However, for events with significant non-DC components, unreasonably lowering the slope angle in the STC inversion using $\kappa = 1$ makes $E_{DC}$ quite large, as shown in Fig. 8(b).

To the contrary, when $\kappa = -0.2$ is used in the STC inversion, the slope angle tends to increase to compensate for the unreasonably low value of $\kappa$ (see eqs 9–11), which results in a smaller DC component, as shown in Figs 7(d) and 8(d).

Comparing Figs 7(d) and 8(d), it can be seen that when the slope angle is 30°, the DC components from the STC inversion using $\kappa = -0.2$ are already close to 0 per cent, which is near the border of the CLVD–ISO diamond plot. Their positions would not change too much even if the slope angles are larger. However, as the true slope angle increases, the true DC component decreases and the true event positions shift towards the borders in the CLVD–ISO diamond plot. Hence, the error $E_{DC}$ reaches the maximum when the slope angle reaches 30°, and then decreases for larger slope angles, as shown in Fig. 3.

The analysis of the behaviours of $E_{\mathrm{ISO}}$ and $E_{\mathrm{CLVD}}$ under different $\kappa$ values and slope angles is similar to the above analysis for $E_{\mathrm{DC}}$, which can be understood together with the intuitive pattern in the CLVD–ISO diamond plots in Figs 7 and 8. A large difference between the inverted and true positions on the horizontal axis of the diamond plot implies a large $E_{\mathrm{CLVD}}$, whereas a large difference in the positions on the vertical axis implies a large $E_{\mathrm{ISO}}$. For example, the results of the STC inversion using $\kappa = -0.2$ are quite different from the true positions on the horizontal axis, which implies a large $E_{\mathrm{CLVD}}$ when the slope angle is 30°, as shown in Fig. 7(d). On the other hand, the results of the STC inversion using $\kappa = 1$ are very close to the true positions on the vertical axis, which implies a small $E_{\mathrm{ISO}}$ even when $E_{\mathrm{CLVD}}$ is very large when the slope angle is 70°, as shown in Fig. 8(b).

For purely shear events, unlike shear-tensile or purely tensile events, values of $\kappa$ too large or too small have no effect on the slope angle based on eqs (9)–(11), so the bias of purely shear events is small and similar for different $\kappa$.

Compared with the three STC inversion strategies, the MT inversion results are more scattered in the diamond plots. However, the scatter is around the true values and a systematic bias is not obvious. Therefore, the biases in the MT inversion results are not always higher than that of the STC inversions using $\kappa = 1$. This indicates that a more concentrated source distribution is not necessarily more accurate.

Fig. 9 shows the distribution of the *P*- and *T*-axes from the four different inversion strategies with a slope angle of 30°. It can be seen that the *P*- and *T*-axes corresponding to the MT inversion are most scattered, especially for the *P*-axis. The *P*- and *T*-axes corresponding to the STC-True inversion are most concentrated. Using a value of $\kappa$ too large ($\kappa = 1$) or too small ($\kappa = -0.2$) in the STC inversion will cause the overall shift of the *P*-axis in different directions. The degree of overall shift depends on the slope angle and $\kappa$, as shown in Fig. 3(d).

## 4 APPLICATION TO FIELD DATA

The West Bohemia region is a seismically active area with a frequent occurrence of earthquake swarms. A high-quality data set including more than 4500 microearthquakes of depths from 6 to 11 km was acquired in 2008–2018 (Vavryčuk *et al.* 2021, 2022). The distribution of the microearthquakes that occurred in 2011 is shown in Fig. 2(a). The double-difference locations (Waldhauser & Ellsworth 2000; Bouchaala *et al.* 2013) of the microearthquakes were determined and the MT inversion based on the principal component analysis (Vavryčuk *et al.* 2017) was applied. 200 microearthquakes are selected and analysed here. The focal mechanisms of the selected microearthquakes are similar and the normalized root-mean-square (RMS) misfit of the *P*-wave amplitudes for each event (Stierle *et al.* 2014b) is smaller than 0.4 (Vavryčuk *et al.* 2021). The MT inversion and the STC-Joint and STC-Vel inversions are performed for the selected microearthquakes to verify the conclusions made from the synthetic experiments described in Section 3. Our STC-Joint inversion obtained a $\kappa$ value of −0.23, indicating a fault zone $V_P/V_S$ value of 1.33, which is very close to the value of −0.2 obtained by Vavryčuk *et al.* (2021) based on thousands of events in 2008–2018. The low $V_P/V_S$ ratio anomalies in this region have also been studied by Bachura & Fischer (2016) and Valentová *et al.* (2017).

Fig. 10 shows the statistics of the DC, CLVD and ISO components and the slope angles of the selected microearthquakes using three different inversion strategies. Slope angles obtained from the MT inversion can be calculated based on eqs (15) and (16), and (6) and (7).

For the STC-Joint inversion, the distributions of the CLVD and ISO components and the slope angle are more concentrated than the results of the MT inversion. More than 80 per cent of the slope angles obtained by the MT and STC-Joint inversions are between −10° and 10°, which means that the non-DC components of the microearthquakes are small. The results of the STC-Vel inversion have the most concentrated DC and CLVD components and the slope angle distributions. More than half of the events have DC components of more than 90 per cent, and only less than one-tenth of the events have DC components less than 80 per cent. The CLVD components obtained by the STC-Vel inversion are all between −20 per cent and 20 per cent, and the slope angles are distributed between −10° and 10°. Even the STC-Vel inversion has such concentrated results. Does this mean that the STC-Vel is the best inversion strategy? The answer is no! The reasons include: (1) based on the statistics of the slope angles in Fig. 10(d), most of the slope angles are between −20° and 10°. The DC components in the results of the STC-Vel inversion are likely to be overestimated, as shown in Fig. 7(b); and (2) the true $\kappa$ value used in the synthetic tests in Fig. 6 is 0.4, and the resulting errors are already obvious for shear-tensile events when $\kappa = 1$ is used in the STC-Vel inversion. If the value of −0.23 obtained by the joint nonlinear inversion is the true $\kappa$ in the West Bohemia region, then $\kappa$ used in the STC-Vel inversion would be much larger than the true value, which results in lower accuracy in the inversion results for all source components.

The distributions and the probability density estimation (Silverman 2018) of the *P*- and *T*-axes (Vavryčuk 2015a) corresponding to the three inversion strategies are shown in Fig. 11. The probability density is computed by using the kernel smoothing function for each point. Larger probability density value means a denser data distribution. Since the RMS of each event is lower than 0.4, the data fit of the MT inversion is very good. Therefore, the distributions of the *P*- and *T*-axes by the MT inversion are relatively concentrated, and the compression and tension regions are clearly separated. The *P*- and *T*-axes from the two STC-based nonlinear inversions are more clustered, and the result from the STC-Joint inversion shows the highest concentration as demonstrated in Fig. 11 by a higher probability density. Combined with the synthetic test results in Fig. 9, we conclude that the *P*- and *T*-axes obtained by the STC-Joint inversion in Fig. 11(b) is the most reliable.

Fig. 10(d) indicates that most of the slope angles for the selected events in the West Bohemia region are between −20° and 10°, which means that results here only pertain to the conclusions in Section 3 for small slope angles. In hydraulic fracturing (Šílený *et al.* 2009; Wang *et al.* 2018; Naoi *et al.* 2020; Li *et al.* 2021b) or volcanic monitoring (Pesicek *et al.* 2012; Kim *et al.* 2014), the non-DC components may be larger. The STC inversion can be more effective than the MT inversion, especially for the DC and CLVD components, as shown in Figs 6(a) and (b).

Here, we only use the *P*-wave amplitudes in the synthetic experiments and in the application to field data. The same analysis can also be applied to the combined use of *P*- and *S*-wave amplitudes (Šílený 2009; Stierle *et al.* 2014b) or to waveform-based inversions (Li *et al.* 2021a).

## 5 CONCLUSIONS

In this study, we carry out a series of synthetic experiments to assess the effectiveness of the STC model in microearthquake focal mechanism inversions. We focus on the performance of the STC model inversion when inappropriate values of $\kappa$ are used. We find that the error of the resulting DC and non-DC components and focal mechanisms can be kept low, provided that an accurate value of $\kappa$ is used. Significantly mistaken values of $\kappa$ may cause large errors in focal mechanisms and lead to wrong interpretations. To prevent this, we propose a joint inversion for both the parameters of the STC model (i.e. strike, dip, rake, slope and magnitude) and $\kappa$. The joint inversion is nonlinear and yields more accurate results than the existing methods. The effectiveness of the STC inversion using an appropriate value of $\kappa$ is improved significantly compared to that of the MT inversion. On the other hand, the STC inversion using $\kappa$ obtained from the $V_P/V_S$ ratio of the crustal velocity model, which has often been used in studies of aftershocks, earthquake swarms, hydraulic fractures and laboratory rock failures, should be avoided.

The conclusions drawn from the synthetic experiments are partly (for small slope angles) verified by applying the MT and STC inversions to microearthquakes in the West Bohemia region. Compared to the MT inversion, both the STC-Joint and STC-Vel inversions yield more concentrated DC and non-DC components as well as focal mechanism solutions. Results indicate that our proposed STC-Joint inversion method is reliable and has a high potential in focal mechanism studies and microearthquake monitoring applications.

## SUPPORTING INFORMATION

Supplementary data are available at *GJI* online.

**Figure S1.** Variations of the errors defined in eqs (29) and (30) with negative slope angles and different $\kappa$ values used in the STC inversions under Scenario I for a true value of $\kappa_0 = 0.4$. Each inversion uses 200 synthetic microearthquakes. (a), (b), (c) and (d) are for $E_{\mathrm{DC}}$, $E_{\mathrm{CLVD}}$, $E_{\mathrm{ISO}}$ and $E_{PT}$, respectively. Note that the colour scales in (a)–(d) are different.

**Figure S2.** (a) Residuals defined in eqs (27) and (28) for different $\kappa$ obtained from Method 3 in synthetic test under Scenario I. The sampling interval of $\kappa$ is 0.01. Solid and dashed lines of different colours represent different slope angles. (b) Zoom-in plot of (a) near minimum residuals. The circle on each line marks the minimum residual. The true value is $\kappa_0 = 0.4$ indicated by the vertical dashed line.

**Figure S3.** Variations of (a) $E_{\mathrm{DC}}$, (b) $E_{\mathrm{CLVD}}$, (c) $E_{\mathrm{ISO}}$ and (d) $E_{PT}$ with the slope angle under Scenario II. Blue lines show the result by the MT inversion. Red, magenta and black lines show results from inversion strategies STC-True, STC-Joint and STC-Vel, respectively. Each inversion uses 200 synthetic microearthquakes. Note that the vertical scales in (a)–(d) are different.

Please note: Oxford University Press is not responsible for the content or functionality of any supporting materials supplied by the authors. Any queries (other than missing material) should be directed to the corresponding author for the article.

## ACKNOWLEDGMENTS

We thank the editor Carl Tape and reviewers Drs. Jiri Zahradnik and Alex Rigby for their critical reviews and detailed comments, which helped improve the manuscript significantly. This work was funded by the National Key R&D Program of China (2020YFA0710600), National Natural Science Foundation of China (U1939202) and the Czech Science Foundation, grant no. 22–10747S. Fig. 2(a) has been produced by GMT of Wessel & Smith (1991). The CLVD–ISO diamond plots have been produced by the public open MATLAB code MT-Decomposition (https://www.ig.cas.cz/en/mt-decomposition/).

## CONFLICT OF INTEREST

All authors declare no conflict of interest regarding the publication of this article.

## DATA AVAILABILITY

The event catalogues and waveforms used for this research are available at https://doi.org/10.17632/4swk36hbvz.1.

## REFERENCES

Aki, K. & Richards, P.G., 2002. *Quantitative Seismology*. New York.

Bachura, M. & Fischer, T., 2016. Detailed velocity ratio mapping during the aftershock sequence as a tool to monitor the fluid activity within the fault plane, *Earth planet. Sci. Lett.,* **453,** 215–222.

Bouchaala, F., Vavryčuk, V. & Fischer, T., 2013. Accuracy of the master-event and double-difference locations: synthetic tests and application to seismicity in West Bohemia, Czech Republic, *J. Seismol,* **17**(3), 841–859.

Byrd, R.H., Gilbert, J.C. & Nocedal, J., 2000. A trust region method based on interior point techniques for nonlinear programming, *Math. Program.,* **89**(1), 149–185.

Červený, V., 2001, *Seismic Ray Theory,* Cambridge Univ. Press, Cambridge, UK.

Chapman, C.H. & Leaney, W.S., 2012. A new moment-tensor decomposition for seismic events in anisotropic media, *Geophys. J. Int.,* **188,** 343–370.

Dahlen, F.A. & Tromp, J., 1998. *Theoretical Global Seismology,* Princeton University Press, Princeton, NJ.

Davi, R., Vavryčuk, V., Charalampidou, E.-M. & Kwiatek, G., 2013. Network sensor calibration for retrieving accurate moment tensors of acoustic emissions, *Int. J. Rock Mech. Mining Sci,* **62,** 59–67.

Dufumier, H. & Rivera, L. 1997. On the resolution of the isotropic component in moment tensor inversion, *Geophys. J. Int.,* **131**(3), 595–606.

Eyre, T.S. & van der Baan, M., 2017. The reliability of microseismic moment-tensor solutions: surface versus borehole monitoring, *Geophysics,* **82**(6), KS113–KS125.

Jechumtálová, Z., Šílený, J. & Málek, J., 2017. The mechanism of microearthquakes related to a gas storage using differently constrained source models: a case study of the Háje location, Czech Republic, *Pure appl. Geophys,* **174**(1), 177–195.

Jechumtálová, Z., Šílený, J. & Trifu, C.I., 2014. Microearthquake mechanism from wave amplitudes recorded by a close-to-surface seismic array at Ocnele Mari, Romania, *Geophys. J. Int,* **197**(3), 1608–1626.

Jost, M.L. & Herrmann, R.B., 1989. A student's guide to and review of moment tensors, *Seismol. Res. Lett,* **60**(2), 37–57.

Kagan, Y.Y., 1991. 3-D rotation of double-couple earthquake sources, *Geophys. J. Int,* **106,** 709–716.

Kim, K., Lees, J.M. & Ruiz, M.C., 2014. Source mechanism of vulcanian eruption at Tungurahua Volcano, Ecuador, derived from seismic moment tensor inversions, *J. geophys. Res.: Solid Earth,* **119,** 1145–1164.

Knopoff, L. & Randall, M.J., 1970. The compensated linear-vector dipole: a possible mechanism for deep earthquakes, *J. geophys. Res,* **75**(26), 4957–4963.

Kozák, J. & Šílený, J., 1985. Seismic events with non-shear component: I. Shallow earthquakes with a possible tensile source component, *Pure appl. Geophys.,* **123**(1), 1–15.

Li, H., Chang, X., Hao, J. & Wang, Y.B., 2021a. The general dislocation source model and its application to microseismic focal mechanism inversion, *Geophysics,* **86**(4), KS79–KS93.

Li, H., Chang, X., Xie, X.B. & Wang, Y.B., 2021b. Microseismic moment-tensor inversion and sensitivity analysis in vertically transverse isotropic media, *Geophysics,* **86**(2), KS23–KS36.

Naoi, M. *et al.*, 2020. Tensile-dominant fractures observed in hydraulic fracturing laboratory experiment using eagle ford shale, *Geophys. J. Int,* **222**(2), 769–780.

Pesicek, J.D., Sileny, J., Prejean, S.G. & Thurber, C.H., 2012. Determination and uncertainty of moment tensors for microearthquakes at Okmok Volcano, Alaska, *Geophys. J. Int,* **190**(3), 1689–1709.

Petružálek, M., Jechumtálová, Z., Kolář, P., Adamová, P., Svitek, T., Šílený, J. & Lokajíček, T., 2018. Acoustic emission in a laboratory: mechanism of microearthquakes using alternative source models, *J. geophys. Res.: Solid Earth,* **123**(6), 4965–4982.

Ren, Y., Gao, Y.T., Wu, S.C. & Vavryčuk, V., 2020. Optimum size and density of surface grid arrays for retrieving accurate shear-tensile fracturing of microearthquakes, *Geophys. Prospect,* **68**(8), 2347–2360.

Ren, Y., Vavryčuk, V., Wu, S.C. & Gao, Y.T., 2021. Accurate moment tensor inversion of acoustic emissions and its application to Brazilian splitting test, *Int. J. Rock Mech. Mining Sci.,* **141,** 104707. doi: 10.1016/j.ijrmms.2021.104707.

Růžek, B. & Horálek, J., 2013. Three-dimensional seismic velocity model of the West Bohemia/Vogtland seismoactive region, *Geophys. J. Int,* **195**(2), 1251–1266.

Růžek, B., Vavryčuk, V., Hrubcová, P. & Zedník, J., Celebration Working Group, 2003. Crustal anisotropy in the Bohemian Massif, Czech Republic: observations based on Central european lithospheric experiment based on refraction (CELEBRATION) 2000, *J. geophys. Res.,* **108**(B8), art. no. 2392. doi: 10.1029/2002JB002242.

Šílený, J., 2009. Resolution of non-double-couple mechanisms: simulation of hypocenter mislocation and velocity structure mismodeling, *Bull. seism. Soc. Am,* **99**(4), 2265–2272.

Šílený, J., Hill, D.P., Eisner, L. & Cornet, F.H., 2009. Non–double-couple mechanisms of microearthquakes induced by hydraulic fracturing, *J. geophys. Res,* **114,** B08307. doi: 10.1029/2008JB005987.

Šílený, J. & Horálek, J., 2016. Shear-tensile crack as a tool for reliable estimates of the non-double-couple mechanism: west Bohemia-Vogtland earthquake 1997 swarm, *Phys. Chem. Earth, Parts a/b/c,* **95,** 113–124.

Šílený, J., Jechumtálová, Z. & Dorbath, C., 2014. Small scale earthquake mechanisms induced by fluid injection at the enhanced geothermal system reservoir Soultz (Alsace) in 2003 using alternative source models, *Pure appl. Geophys,* **171**(10), 2783–2804.

Šílený, J., Panza, G.F. & Campus, P., 1992. Waveform inversion for point source moment tensor retrieval with variable hypocentral depth and structural mode, *Geophys. J. Int,* **109**(2), 259–274.

Šílený, J. & Vavryčuk, V., 2002. Can unbiased source be retrieved from anisotropic waveforms by using an isotropic model of the medium?, *Tectonophysics,* **356,** 125–138.

Silverman, B.W., 2018. *Density Estimation for Statistics and Data Analysis*. Routledge.

Stierle, E., Bohnhoff, M. & Vavryčuk, V., 2014a. Resolution of non-double-couple components in the seismic moment tensor using regional networks—II: application to aftershocks of the 1999 Mw 7.4 Izmit earthquake, *Geophys. J. Int,* **196**(3), 1878–1888.

Stierle, E., Vavryčuk, V., Kwiatek, G., Charalampidou, E.-M. & Bohnhoff, M., 2016. Seismic moment tensors of acoustic emissions recorded during laboratory rock deformation experiments: sensitivity to attenuation and anisotropy, *Geophys. J. Int,* **205**(1), 38–50.

Stierle, E., Vavryčuk, V., Šílený, J. & Bohnhoff, M., 2014b. Resolution of non-double-couple components in the seismic moment tensor using regional networks—I: a synthetic case study, *Geophys. J. Int,* **196**(3), 1869–1877.

Tape, W. & Tape, C., 2012a. A geometric setting for moment tensors, *Geophys. J. Int,* **190,** 476–498.

Tape, W. & Tape, C., 2012b. A geometric comparison of source-type plots for moment tensors, *Geophys. J. Int,* **190,** 499–510.

Tape, W. & Tape, C., 2013. The classical model for moment tensors, *Geophys. J. Int,* **195**(3), 1701–1720.

Valentová, L., Gallovič, F. & Maierová, P., 2017. Three-dimensional S-wave velocity model of the Bohemian Massif from bayesian ambient noise tomography, *Tectonophysics,* **717,** 484–498.

Vavryčuk, V., 2001. Inversion for parameters of tensile earthquakes, *J. geophys. Res,* **106**(B8), 16,339–316,355.

Vavryčuk, V., 2011. Tensile earthquakes: theory, modeling, and inversion, *J. geophys. Res,* **116**(B12), B12320. doi: 10.1029/2011JB008770.

Vavryčuk, V., 2015a. Moment tensor decompositions revisited, *J. Seismol,* **19**(1), 231–252,

Vavryčuk, V., 2015b. Inversion for the composite moment tensor, *Bull. seism. Soc. Am,* **105**(6), 3024–3035.

Vavryčuk, V., Adamová, P., Doubravová, J. & Horálek, J., 2022. Moment tensor catalogue of earthquakes in West Bohemia from 2008 to 2018, *Earth Syst. Sci. Data,* **14,** 2179–2194.

Vavryčuk, V., Adamová, P., Doubravová, J. & Jakoubková, H., 2017. Moment tensor inversion based on the principal component analysis of waveforms: method and application to microearthquakes in West Bohemia, Czech Republic, *Seismol. Res. Lett,* **88**(5), 1303–1315.

Vavryčuk, V., Adamová, P., Doubravová, J. & Ren, Y., 2021. Mapping stress and fluids on faults by nonshear earthquakes, *J. geophys. Res.: Solid Earth,* **126,** e2020JB021287. doi: 10.1029/2020JB021287.

Vavryčuk, V. & Hrubcová, P., 2017. Seismological evidence of fault weakening due to erosion by fluids from observations of intraplate earthquake swarms, *J. geophys. Res.: Solid Earth,* **122**(5), 3701–3718.

Waldhauser, F. & Ellsworth, W.L., 2000. A double-difference earthquake location algorithm: method and application to the northern Hayward fault, California, *Bull. seism. Soc. Am.,* **90**(6), 1353–1368.

Wang, R., Gu, Y.J., Schultz, R. & Chen, Y.F., 2018. Faults and non-double-couple components for induced earthquakes, *Geophys. Res. Lett,* **45**(17), 8966–8975.

Weisberg, S., 2013. *Applied Linear Regression*. John Wiley & Sons.

Wessel, P. & Smith, W.H.F., 1991. Free software helps map and display data, *EOS Trans. Am. geophys. Un.,* **72,** 441–446.

Yu, C., Vavryčuk, V., Adamová, P. & Bohnhoff, M., 2018. Moment tensors of induced microearthquakes in the Geysers geothermal reservoir from broadband seismic recordings: implications for faulting regime, stress tensor, and fluid pressure, *J. geophys. Res.: Solid Earth,* **123,** 8748–8766.

Zhang, H., Eaton, D.W., Rodriguez, G. & Jia, S.Q., 2019. Source-mechanism analysis and stress inversion for hydraulic-fracturing-induced event sequences near Fox Creek, Alberta, *Bull. seism. Soc. Am,* **109**(2), 636–651.

Zhu, L. & Ben-Zion, Y., 2013. Parametrization of general seismic potency and moment tensors for source inversion of seismic waveform data, *Geophys. J. Int,* **194**(2), 839–843.